

Supplementary Material
To
Activation of SrTiO₃ with subsurface SrRuO₃ for Oxygen Evolution Reaction

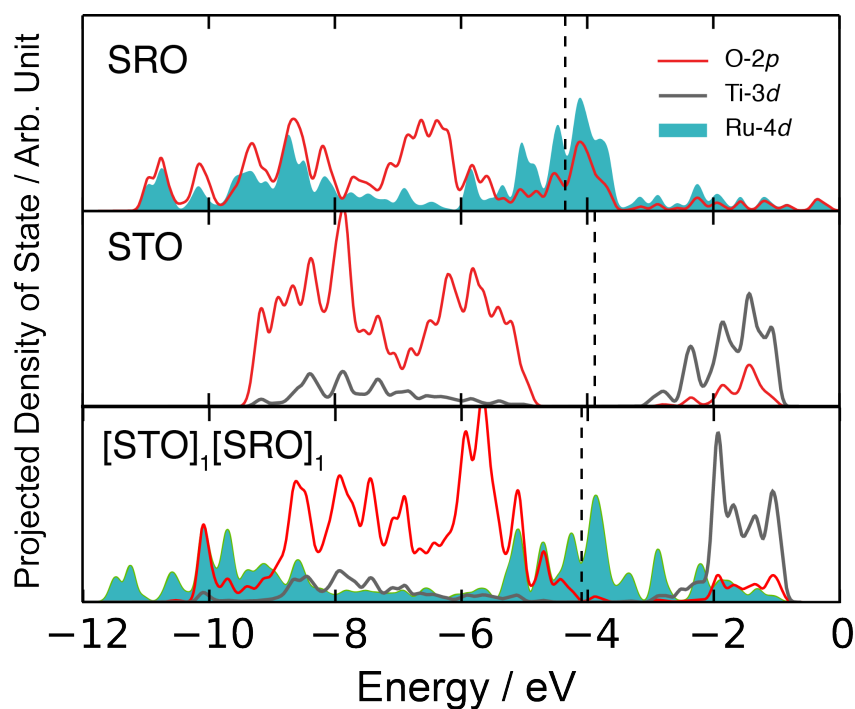
A.R. Akbashev^{1,*}, L. Zhang^{2,*}, J. Tyler Mefford¹, J. Park¹, B. Butz¹, H. Luftman³, W.C. Chueh^{1,†},
A. Vojvodic^{2,†}
(* these authors contributed equally to this work)

¹ Department of Materials Science and Engineering, Stanford University, Stanford, CA
94305, USA

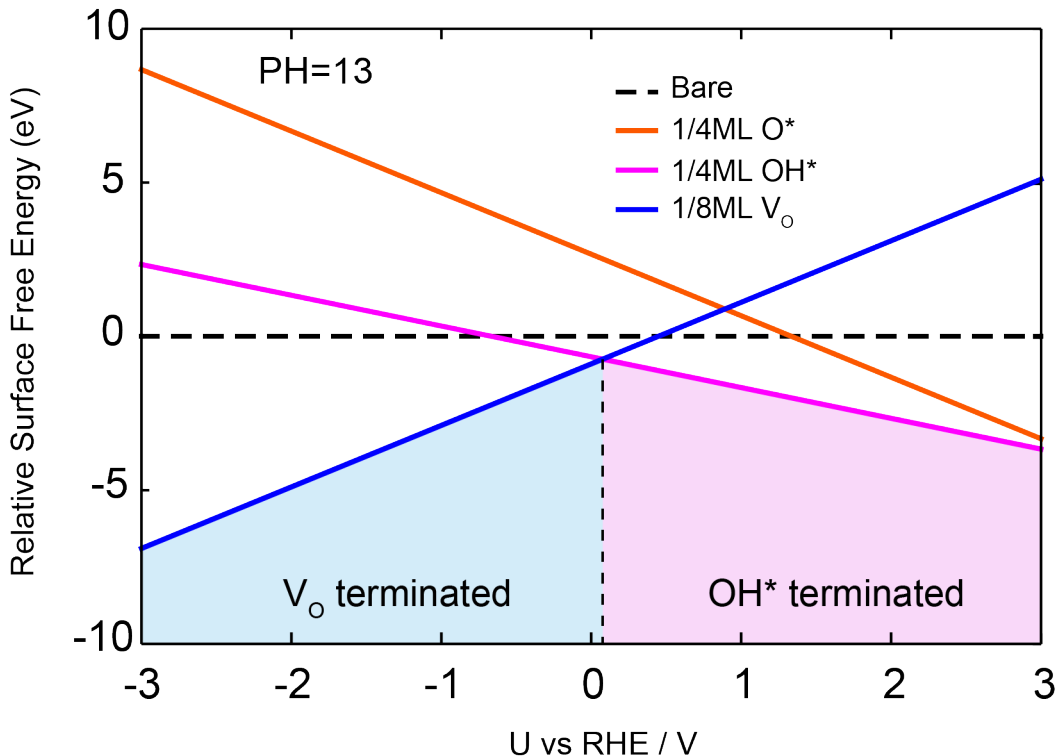
² Department of Chemical and Biomolecular Engineering, University of Pennsylvania,
Philadelphia, Pennsylvania 19104, USA

³ Surface Characterization Facility, Lehigh University, Bethlehem, Pennsylvania 18105, USA

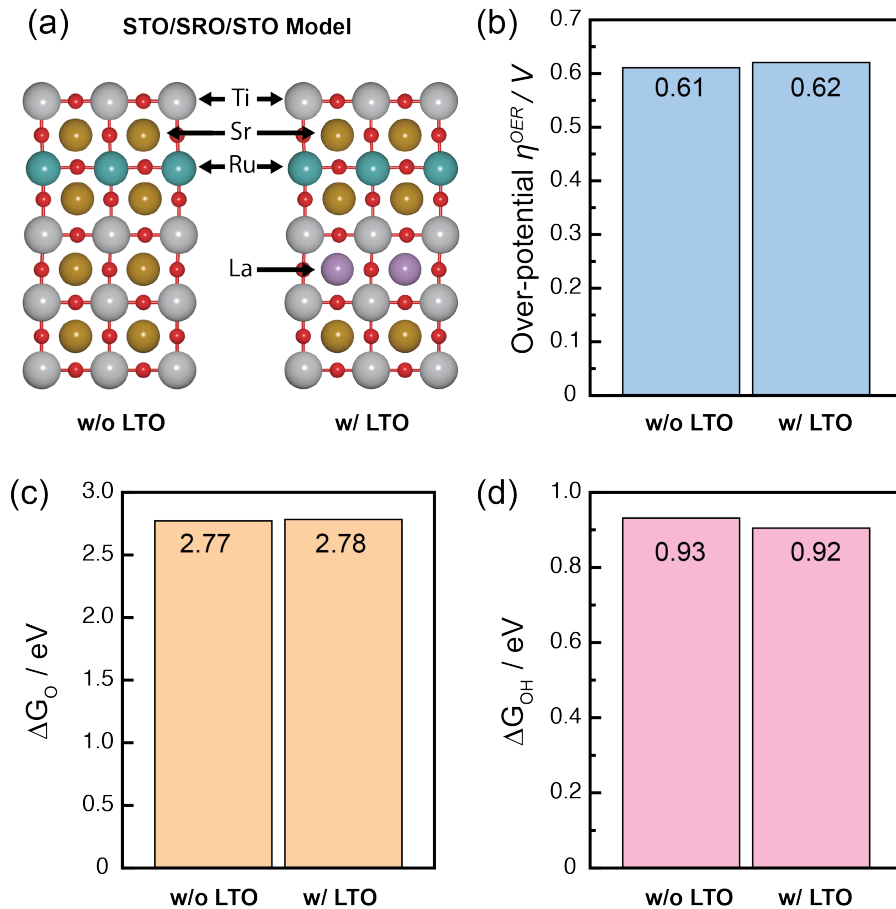
1. Additional data and results from *ab initio* calculations



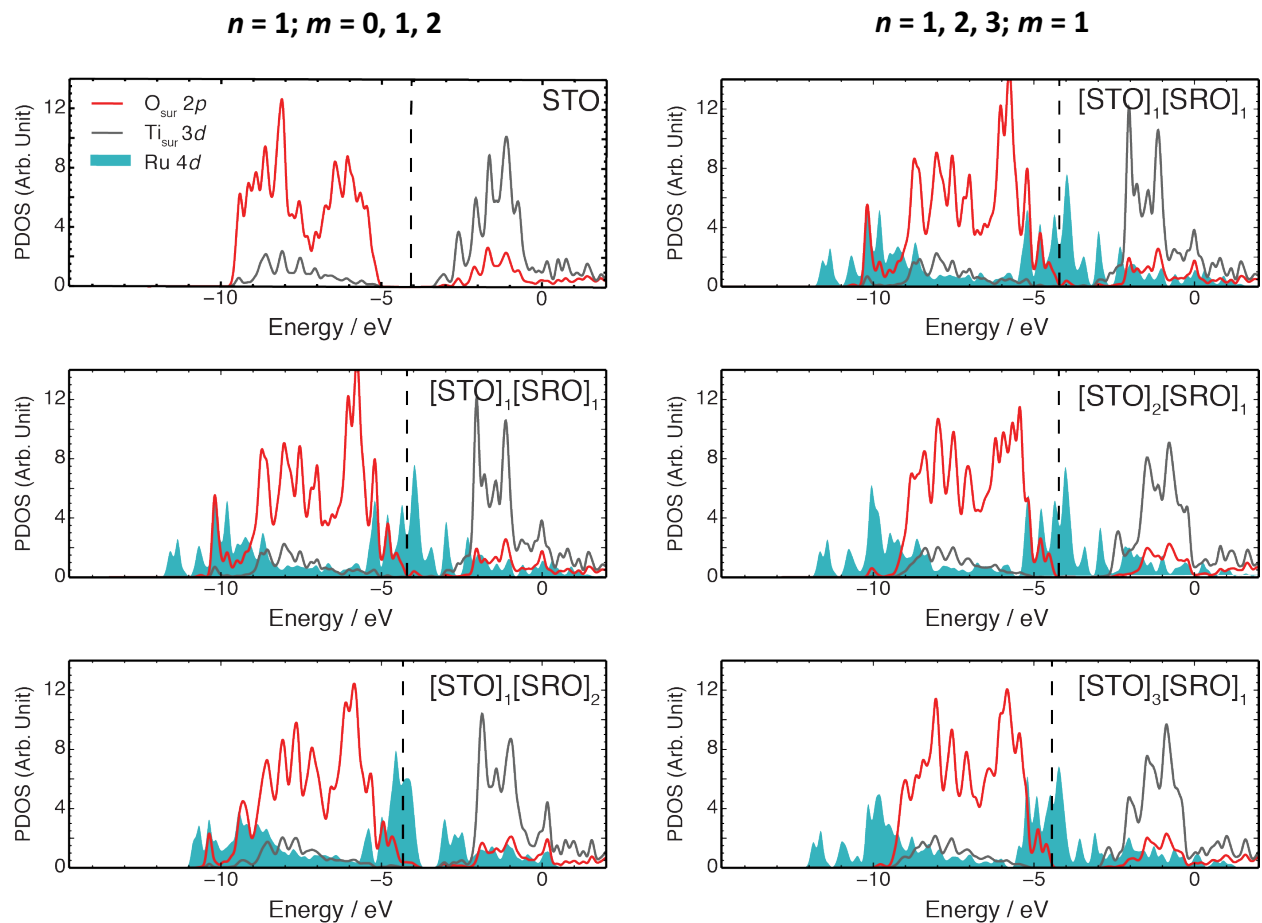
Extended Data Figure 1. DFT calculated projected density of states (PDOS) of the STO, SRO and [STO]₁[SRO]₁ (001) surface systems. 2p states of lattice O in the first surface layer, surface Ti 3d, and Ru 4d states are plotted as red, grey, and cyan filled lines, respectively. All energies are referenced to the vacuum level, the Fermi level for each system is indicated as a vertical black dashed line.



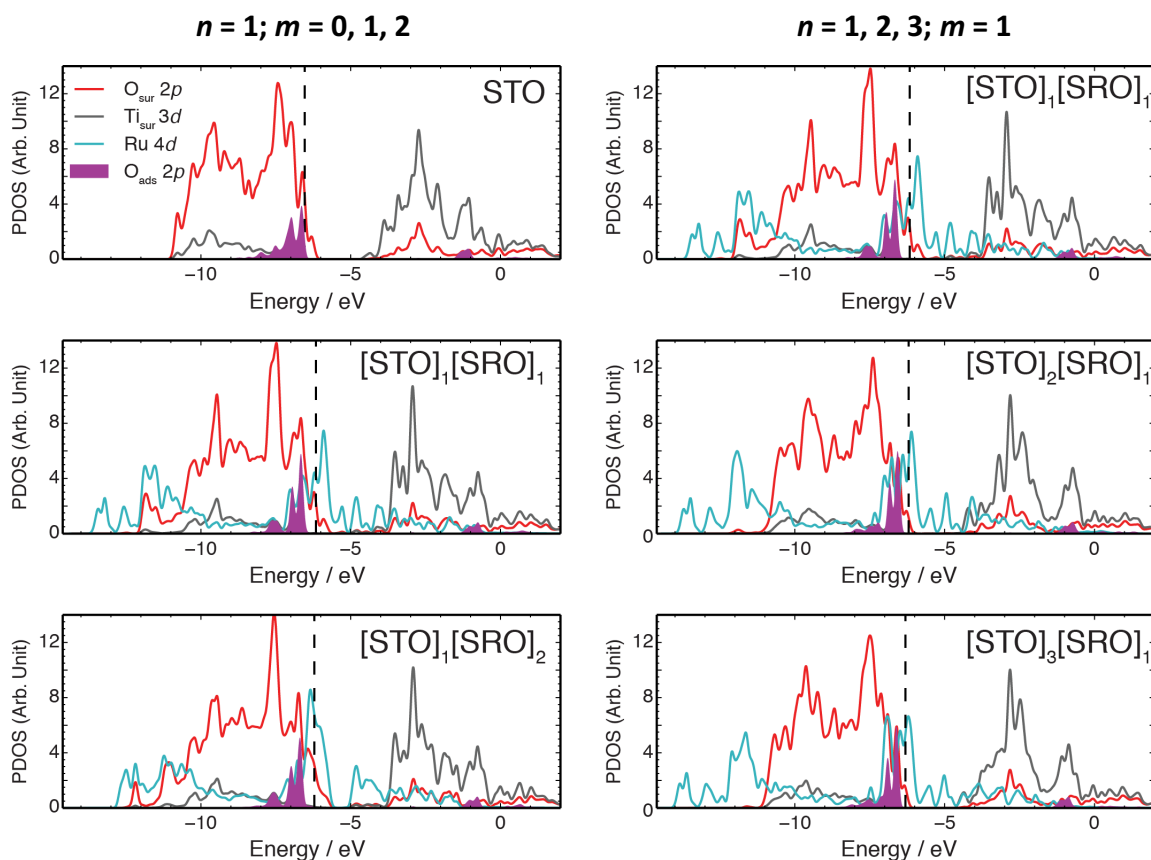
Extended Data Figure 2. Calculated phase diagram of the [STO]₁[SRO]₁ (001) surface as a function of the potential at pH=13. The notation: bare, O*, OH* and V_O in the figure legend represent the stoichiometric surface, 1/4 ML O-covered surface, 1/4 ML OH-covered surface and the surface with 1/8 ML O vacancies in the first surface layer. Under OER conditions, formation of O vacancies is not favored. In addition, we find that the A₁ like intermediate in Ref. 1 where O₂ adsorbing on top of a Ti atom neighboring an O vacancy is not a stable geometry. This implies that the preferred OER mechanism for this system is the adsorbate-mediated pathway rather than the lattice-oxygen mediated pathway as has been suggested in other systems (see, for example, Ref. 1).



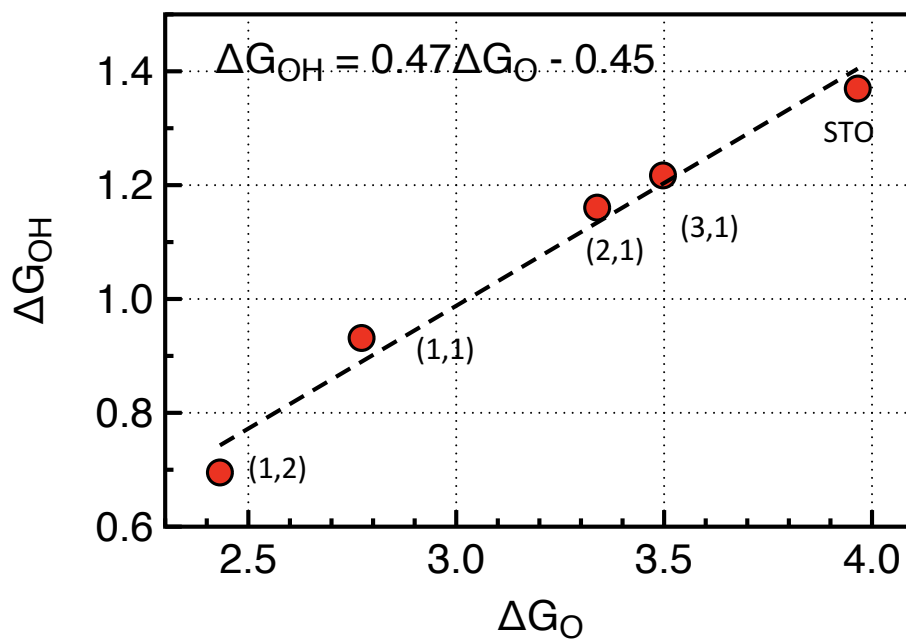
Extended Data Figure 3. (a) Two different computational models of $[STO]_1[SRO]_1$ without and with a $LaTiO_3$ (LTO) layer. Presence of an explicit LTO layer has no significant effect (< 0.01 eV) on the surface chemistry in terms of (b) theoretical OER overpotential, (c) free energy of O adsorption ΔG_O , and (d) free energy of OH adsorption ΔG_{OH} .



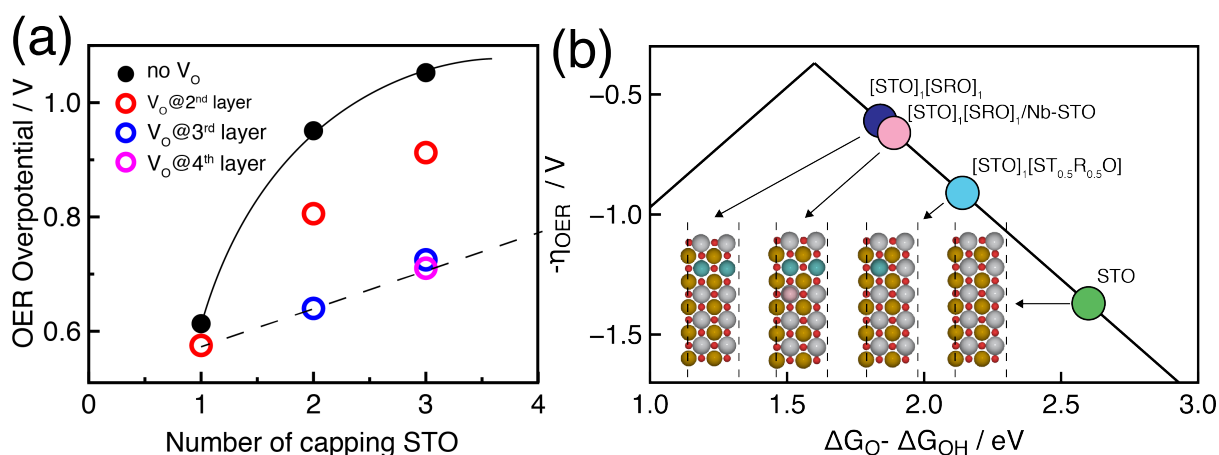
Extended Data Figure 4. DFT calculated projected density of states (PDOS) of bare $[STO]_n[SRO]_m$ (001) surfaces with different n and m . $2p$ states of lattice O in the first surface layer, surface Ti $3d$, and Ru $4d$ states are plotted as red, grey solid lines and cyan filled lines, respectively. All energies are referenced to the vacuum level, the Fermi level for each system is indicated as a vertical black dashed line.



Extended Data Figure 5. DFT calculated projected density of states (PDOS) of the systems where O is adsorbed on the $[\text{STO}]_n[\text{SRO}]_m$ (001) surface with different n and m . $2p$ states of lattice O in the first surface layer, surface Ti $3d$, Ru $4d$, and the oxygen adsorbate $2p$ states are plotted as red, grey, cyan solid lines and purple filled lines, respectively. All energies are referenced to the vacuum level, the Fermi level for each system is indicated as a vertical black dashed line.



Extended Data Figure 6. Linear adsorbate energy scaling fit (black dashed line) between DFT calculated (red circles) OH^* and O^* adsorption free energies ΔG_{OH} and ΔG_{O} , respectively, on the $[\text{STO}]_n[\text{SRO}]_m$ (001) surfaces with different n and m denoted as (n, m) .



Extended Data Figure 7. (a) Theoretical OER overpotentials of $[STO]_n[SRO]_1$ (001) surface with and without O vacancy. Solid dots stand for stoichiometric structures, while open circles represent for structures with one single O vacancy at different layer. Various positions of O vacancy are highlighted with different colors. Dashed line connects the lowest OER-overpotential of given number of STO capping layers. (b) DFT calculated OER overpotential of $[STO]_1[SRO]_1$, $[STO]_1[SRO]_1/Nb-STO$, $[STO]_1[ST_{0.5}R_{0.5}O]$, and STO as a function of the standard free energy difference $\Delta G_{O^-} - \Delta G_{OH}$. The inset shows the unit cell of corresponding structures.

$[STO]_1[SRO]_1/Nb-STO$ uses $[STO]_1[SRO]_1$ with one Ti atom (out of 4) replaced by a Nb atom in the third layer from the surface. We found that the OER overpotential is only increased by 0.05 V. Noteworthy, such a model structure has the Nb atom in the closest possible position to the surface (right under the SRO unit cell), with an “in-plane concentration” of 25%. Because the Nb doping level is $\sim 1\%$ in real substrates and the Nb dopants are evenly distributed in the entire substrate, the DFT calculation models an upper limit on the activity change due to the Nb doping.

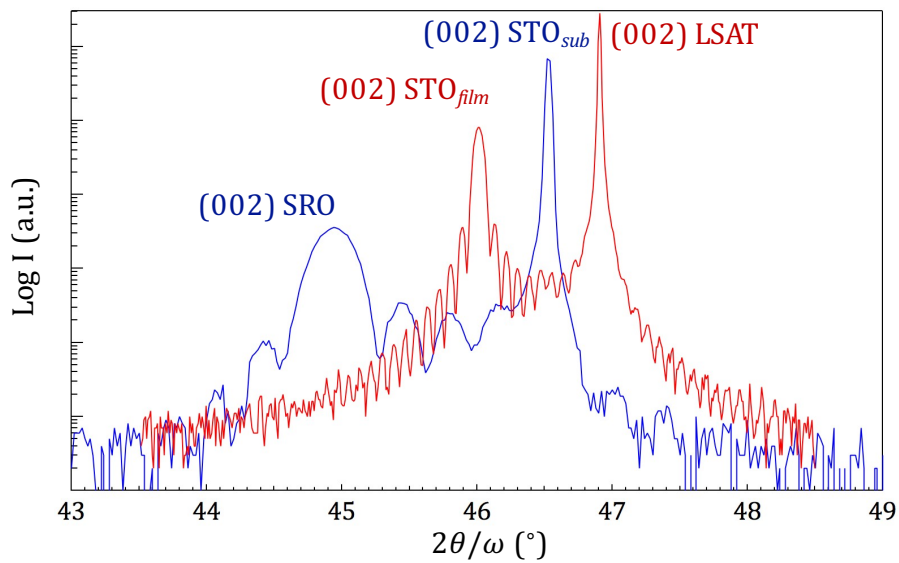
In the case of $[STO]_1[ST_{0.5}R_{0.5}O]$, our calculations of the intermixing of Ti and Ru in the subsurface region show a reduction in the activation effect due to Ru, since less charge is transferred from the subsurface Ru to the adsorbate on the surface. In other words, a higher Ti concentration due to intermixing will lead to a weaker binding of the adsorbates and, hence, result in a higher OER overpotential. For example, when the Ti:Ru mixing ratio is 1:1 in the subsurface (denoted $[STO]_1[ST_{0.5}R_{0.5}O]$ in our notation), the OER overpotential increases from 0.61 to 0.96 V as compared to $[STO]_1[SRO]_1$. Hence, the fact that we observe a low OER overpotential also indicates that the intermixing is small.

Extended Data Table 1. Calculated charge difference (units of electrons) of all Ru atoms in the SRO layer(s) ($\Delta\rho_{\text{SRO}}$), all Ti atoms in the capping STO layer(s) ($\Delta\rho_{\text{STO}}$), and adsorbed O ($\Delta\rho_{\text{O}_{\text{ads}}}$), during O adsorption on the surface of the $[\text{STO}]_n[\text{SRO}]_m$ (001) surface systems with different n and m as obtained by Bader analysis. $\Delta\rho_{\text{STO}}$ and $\Delta\rho_{\text{SRO}}$ is the charge corresponding associated with the entire layer(s). Donating and accepting of elections are marked as negative and positive numbers, respectively.

System	$\Delta\rho_{\text{SRO}}$	$\Delta\rho_{\text{STO}}$	$\Delta\rho_{\text{O}_{\text{ads}}}$	$\Delta\rho_{\text{SRO}} + \Delta\rho_{\text{STO}}$
STO	-	-0.76	0.72	-0.76
$[\text{STO}]_1[\text{SRO}]_1$	-0.17	-0.57	0.73	-0.74
$[\text{STO}]_2[\text{SRO}]_1$	-0.06	-0.66	0.73	-0.72
$[\text{STO}]_3[\text{SRO}]_1$	-0.04	-0.68	0.72	-0.72
$[\text{STO}]_1[\text{SRO}]_2$	-0.19	-0.57	0.74	-0.76

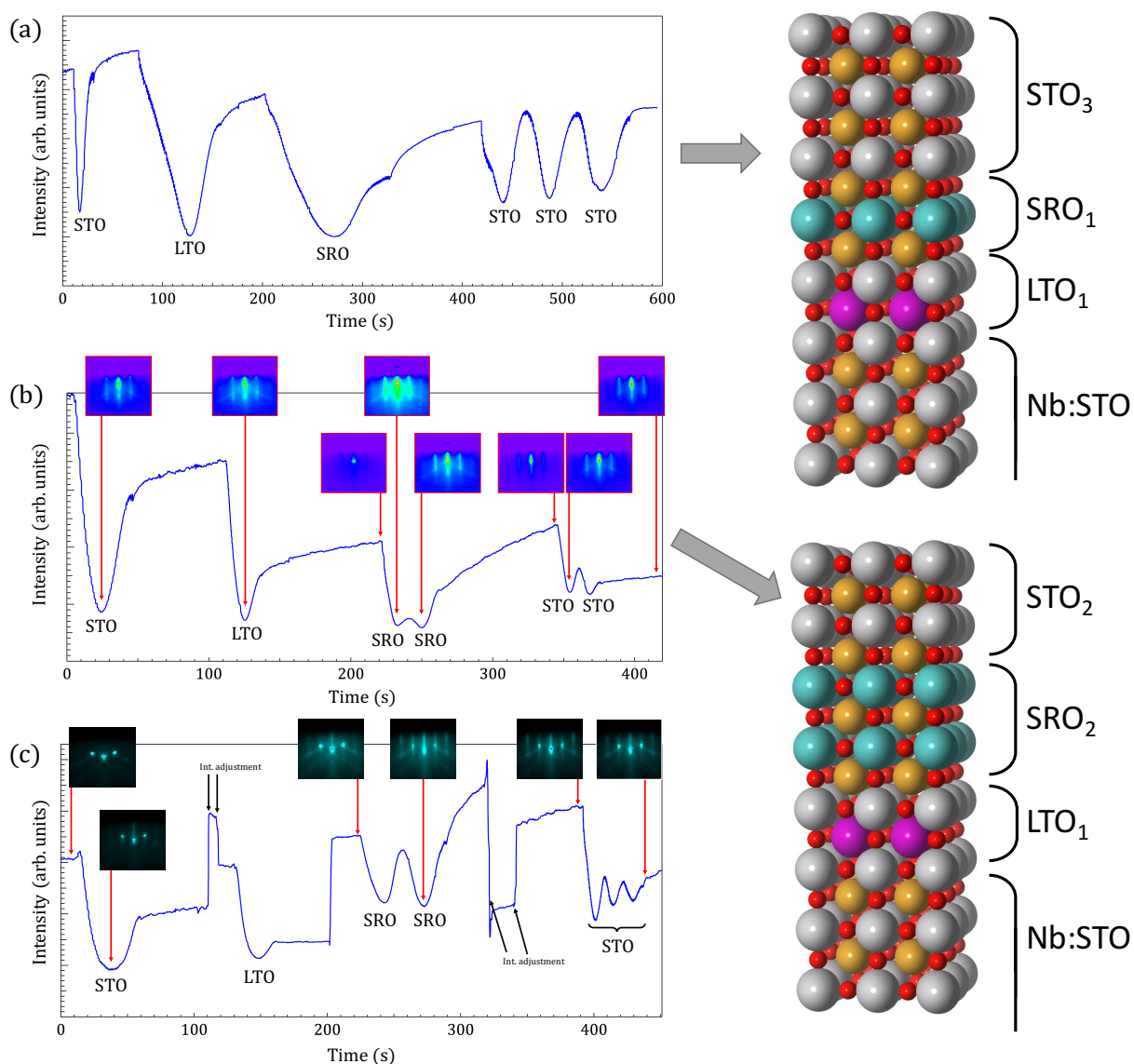
2. Additional Characterization

XRD patterns of the individual SrTiO₃ and SrRuO₃ thin films are shown in **Extended Data Figure 8**. We use the (LaAlO₃)₃(Sr₂AlTaO₆)₇ (LSAT) substrate because the SrTiO₃ film on the SrTiO₃ substrate will be indistinguishable (the substrate and the film peaks will have the same Bragg position). Lattice constants calculated from the (002) peaks are $c_{\text{STO}} = 3.94 \text{ \AA}$ and $c_{\text{SRO}} = 4.03 \text{ \AA}$. In both cases the substrates impose a small compressive strain ($\epsilon_{\text{SRO}} = -0.6 \%$, $\epsilon_{\text{STO}} = -0.9 \%$; $a_{\text{SRO}}^{\text{pseudocub.}} = 3.930 \text{ \AA}$, $a_{\text{STO}} = 3.905 \text{ \AA}$, $a_{\text{LSAT}} = 3.868 \text{ \AA}$) resulting in larger out-of-plane lattice parameters than in the bulk state.

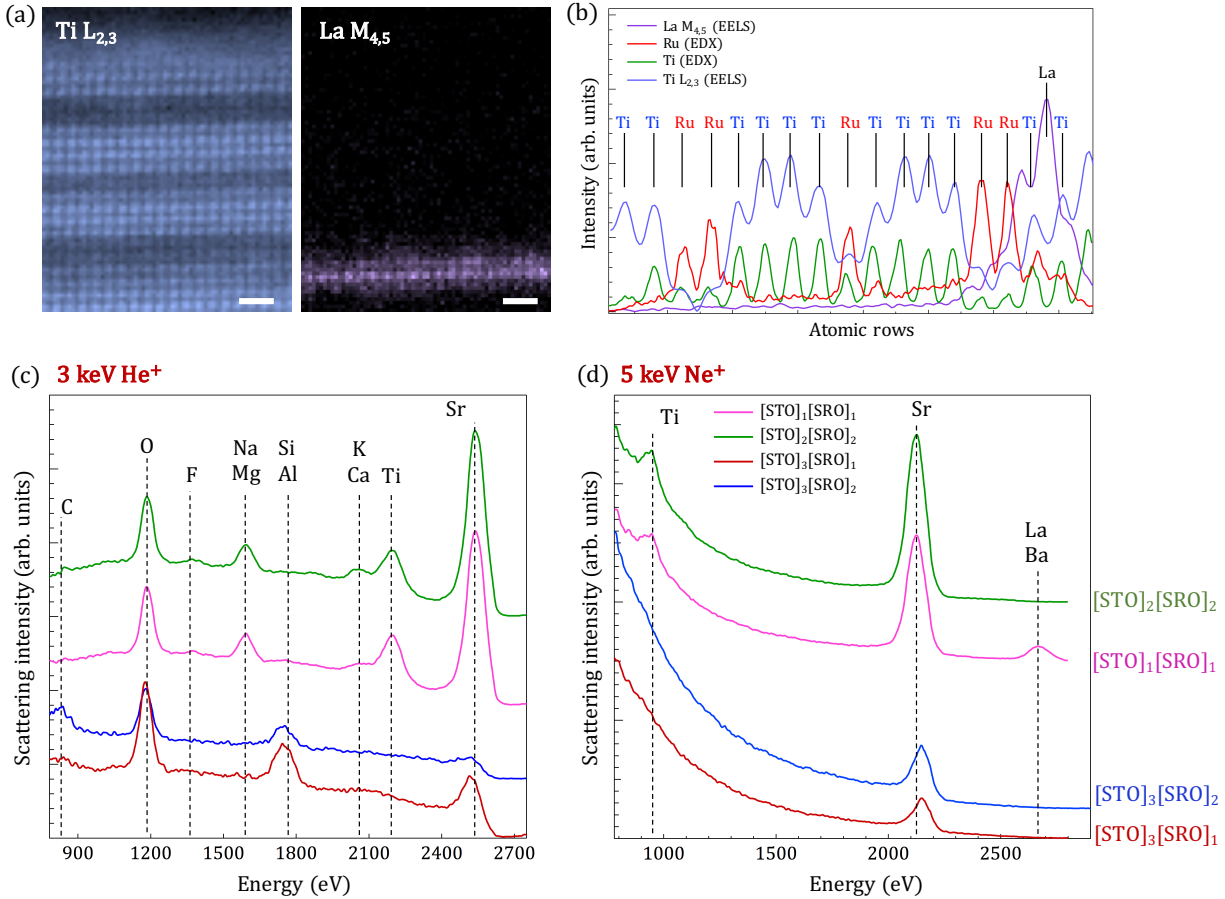


Extended Data Figure 8. X-ray diffraction of the (001) SrTiO₃ film on (001) LSAT and (001) SrRuO₃ on (001) SrTiO₃.

However, we should note that, strictly speaking, the XRD of such thin films (thickness over 10 nm) is not representative of the layers comprising only few unit cell. Therefore, we relied on the combination of RHEED patterns, LEIS and (S)TEM results to assess the quality of the $[\text{STO}]_n[\text{SRO}]_m$ ultrathin heterostructures (**Extended Data Figure 9-10**).



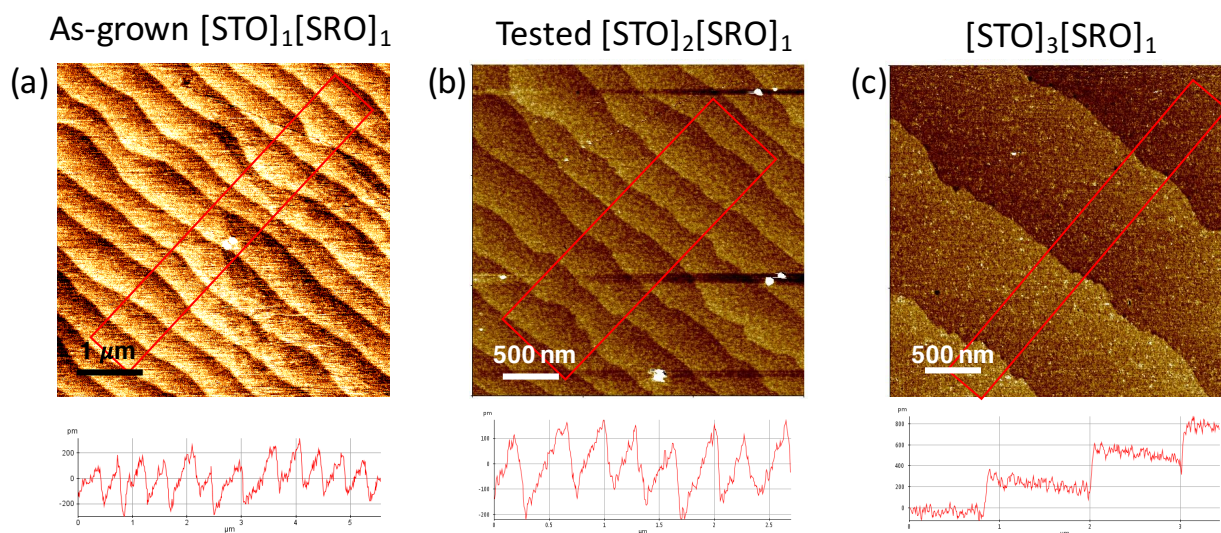
Extended Data Figure 9. Examples of the RHEED intensity oscillations (specular spot) during the growth of the $[\text{STO}]_3[\text{SRO}]_1$, $[\text{STO}]_2[\text{SRO}]_2$ and $[\text{STO}]_2[\text{SRO}]_3$ heterostructures. The red arrows connect the RHEED images to the respective time during the growth. The structures for $[\text{STO}]_2[\text{SRO}]_2$ and $[\text{STO}]_2[\text{SRO}]_3$ are given on the right.



Extended Data Figure 10. (a) EELS maps for Ti L_{2,3} and La M_{4,5} edges. The specimen is the same as in Figure 2(a), but the region is different. (b) The profiles of atomic columns integrated along the layers in (a) and Figure 2(a). Because the regions for EDX and EELS collection are different, the profiles are aligned with respect to each other. (c-d) Low-energy ion scattering spectra for different as-grown [STO]_n[SRO]_m heterostructures. (c) 3-keV He⁺ spectra (sensitive to lighter elements) show typical surface contamination of oxides when exposed to air (including sample shipping), which was also observed by LEIS in other studies²⁻⁴. (d) 5-keV Ne⁺ spectra (sensitive to heavier elements) showing the presence of Ti and Sr on the surface. In few samples a heavier element (La or Ba) was observed, the origin of which is unclear.

In **Extended Data Figure 10(a)** we show EELS maps of Ti and La for the same sample as in Figure 2(a). The elemental profiles are given in **Extended Data Figure 10(b)**. Here we should note that the growth of heterostructures with a unit cell precision is never free of interdiffusive processes, especially for the same crystal structures (a perovskite on a perovskite). Moreover, the complexity of the growth and thermodynamic instability of the resulting layers can contribute to the interdiffusion. Similar mild chemical intermixing was observed in the samples grown by the state-of-the-art PLD and molecular beam epitaxy systems (see, for example, Ref. 5-8 and Supplementary Information in Ref. 9 and 10).

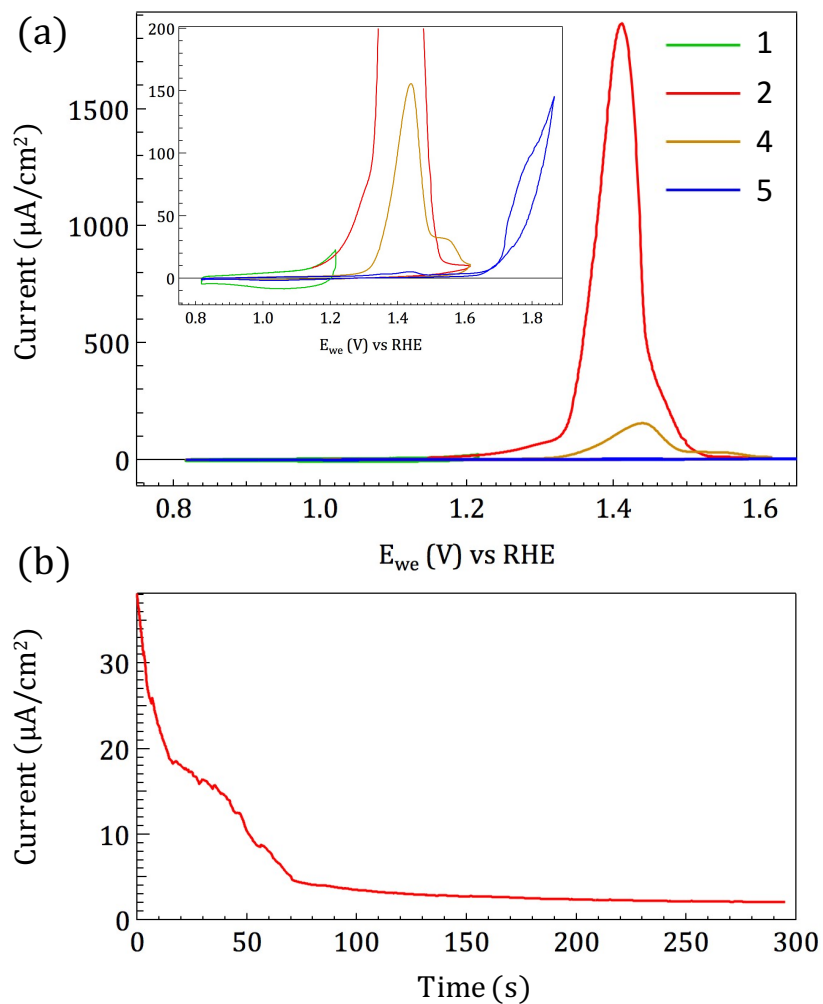
AFM imaging of the heterostructures tested for a prolonged period (up to 24-28 h) shows that the OER-active samples have the expected 1-unit-cell-step terraces without any pinholes (**Extended Data Figure 11**), as expected in the case of surface preservation during OER.



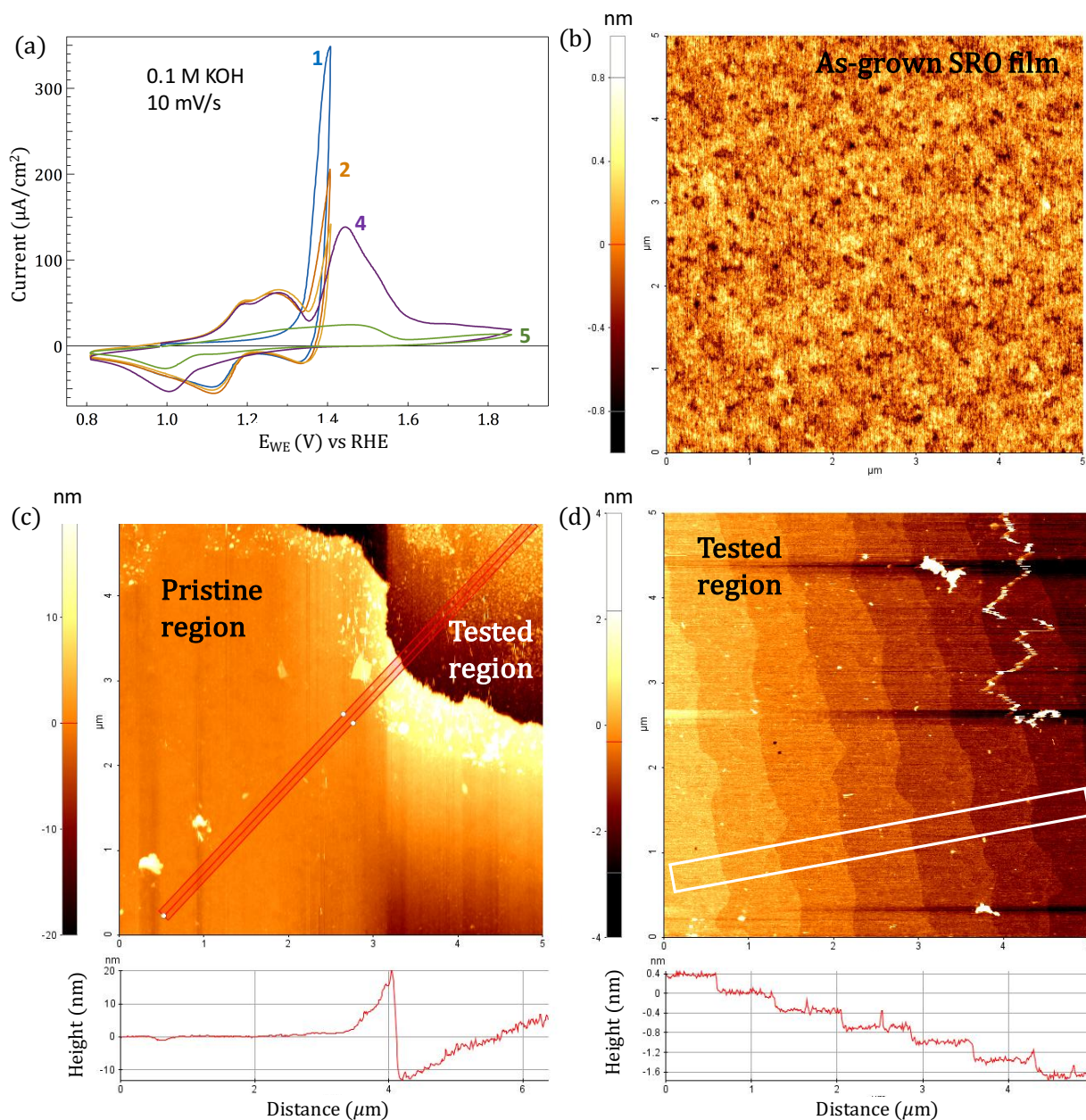
Extended Data Figure 11. AFM images of the $[\text{STO}]_n[\text{SRO}]_m$ heterostructures: (a) as-grown and (b) electrochemically tested for a prolonged time. The height of the terraces is one unit cell (~ 0.4 nm).

Typical electrochemical behavior of SrRuO_3 thin films is given in **Extended Data Figure 12-13**. The dissolution presumably starts at 1.3-1.4 V vs RHE and is indicated by a sharp raise of current that goes through a maximum upon further increase of potential. This behavior was also reported by Chang *et al.*¹¹ During potential hold, the current drops to few $\mu\text{A}/\text{cm}^2$.

The dissolution of pure SrRuO_3 thin films during OER was probed *ex situ* with AFM, *i.e.*, we performed the imaging of the as-grown SrRuO_3 film and then after electrochemical tests. The results are given in **Extended Data Figure 13**. At first, the surface of the film roughens and reveals grains, which implies that the dissolution is preferable at the grain boundaries. Next, after 24-hour-long OER tests (overpotential is 0.63 V), the sample shows only step terraces of the substrate that are left after the complete dissolution of SrRuO_3 film. At the boundary between the dissolved area and the electrolyte-unexposed area, the drop of height is close to the thickness of the SrRuO_3 film (~ 30 nm).

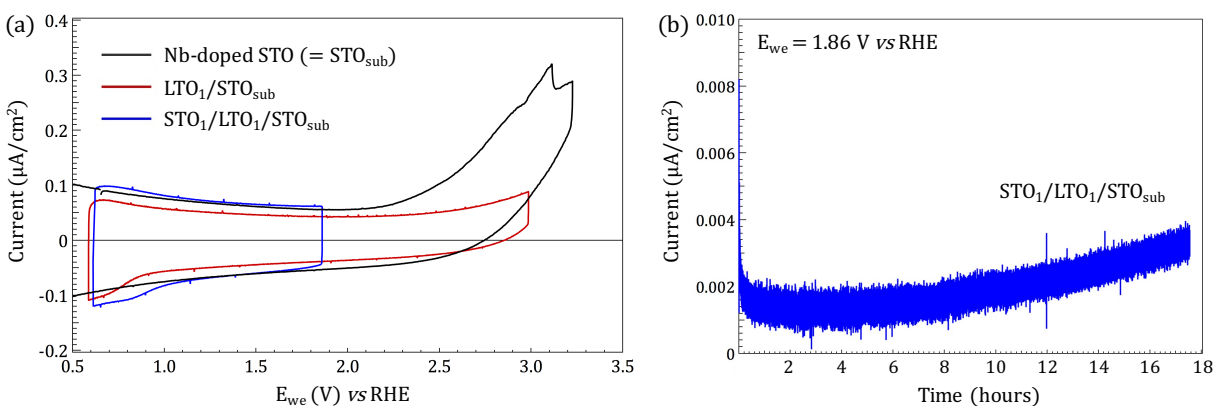


Extended Data Figure 12. (a) CV of the 30-nm (001) SrRuO₃ film grown on LTO₁/STO_{sub}. The numbers in the plot denote the cycle numbers. The inset shows the same plot, but with smaller currents. The scanning rate was 10 mV/s. (b) Time-dependent current measured during potentiostatic hold (overpotential 0.64 V).

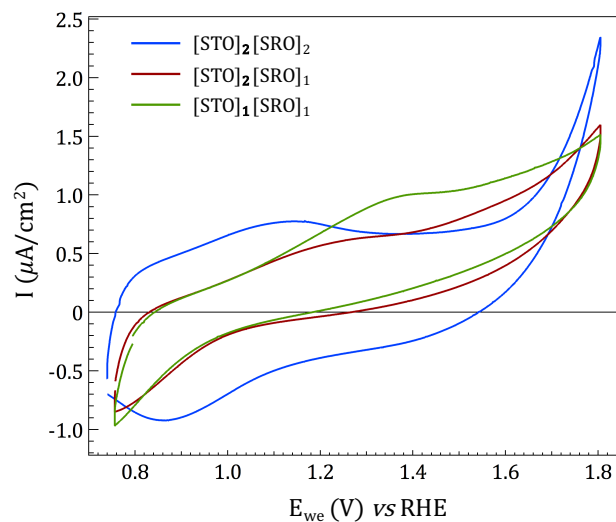


Extended Data Figure 13. (a) CV of the 30 nm thick (001) SrRuO₃ film grown on LTO₁/STO_{sub}. The numbers in the plot denote the cycle numbers. After the 5th cycle, the sample underwent a potentiostatic measurement (0.63 V) for 24 h. (b) The untested region of the SrRuO₃ film. (c) The boundary between the untested and tested regions, showing the height drop that signifies dissolution in the tested region. (d) The middle of the tested region showing the step terraces (1 u.c. height) of the substrate without any noticeable residuals of SrRuO₃ after the potentiostatic experiment.

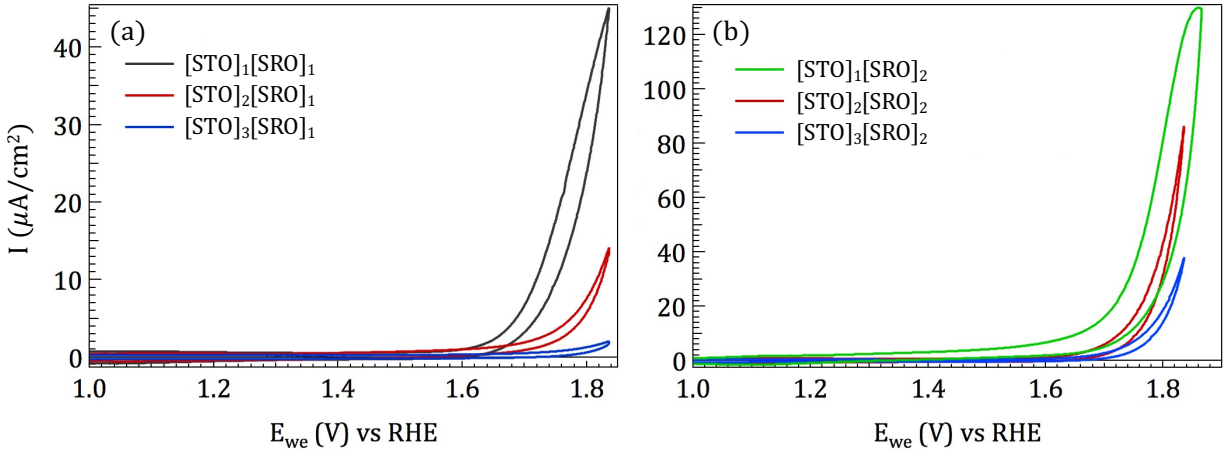
Cyclic voltammetry of the 1-u.c. thick LTO layer and $\text{STO}_1/\text{LTO}_1$ heterostructure on the Nb:STO substrate (with a 1-u.c. STO_1 layer grown on top of the substrate for the surface restoration) is provided in the **Extended Data Figure 14(a)**. The capacitive current is below $0.1 \mu\text{A}/\text{cm}^2$ and shows no noticeable OER onset. To evaluate the behavior of the $\text{STO}_1/\text{LTO}_1/\text{STO}_{\text{sub}}$ (*i.e.*, nominally the $[\text{STO}]_1[\text{SRO}]_0$ sample) we perform an ~ 18 h potentiostatic measurement (**Extended Data Figure 14(b)**). The current stays at a few nA/cm^2 , indicating a completely inert behavior toward OER. We also do not see any niobium oxide segregation on the surface after the substrate preparation and treatment, as expected from a number of studies (see, for example, Ref. ¹²).



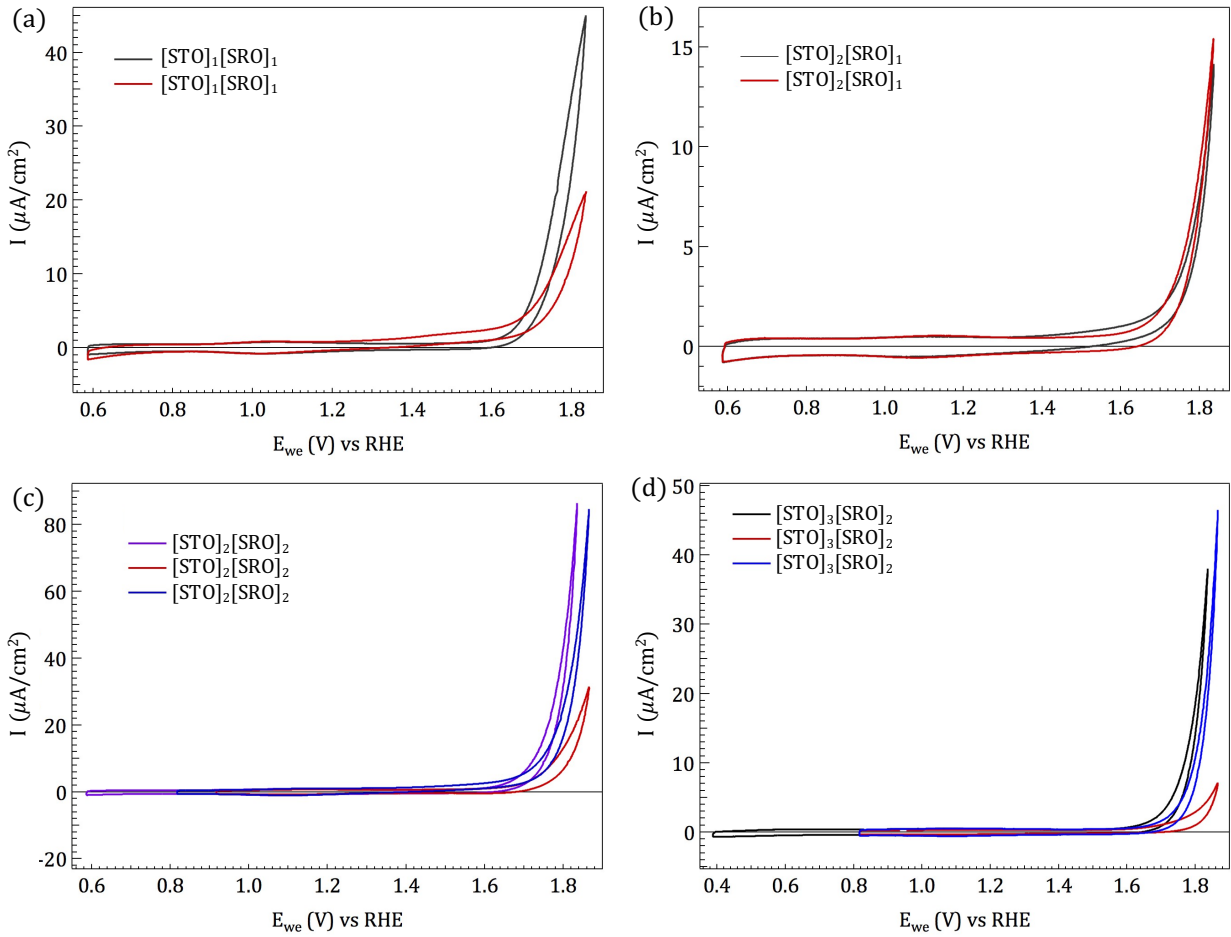
Extended Data Figure 14. (a) CV curves of Nb-doped STO (same as bare STO_{sub}), $\text{LTO}_1/\text{STO}_{\text{sub}}$ and $\text{STO}_1/\text{LTO}_1/\text{STO}_{\text{sub}}$. (b) Potentiostatic measurement ($E_{\text{we}} = 1.86$ V vs RHE) of the $\text{STO}_1/\text{LTO}_1/\text{STO}_{\text{sub}}$ sample. Scan rates are 10 mV/s.



Extended Data Figure 15. CV curves of $[\text{STO}]_1[\text{SRO}]_1$, $[\text{STO}]_2[\text{SRO}]_1$ and $[\text{STO}]_2[\text{SRO}]_2$ grown on the STO_{sub} without the LTO_1 sublayer. A low anodic current at high potential is the result of the Schottky junction between SRO and STO. Scan rates are 10 mV/s.

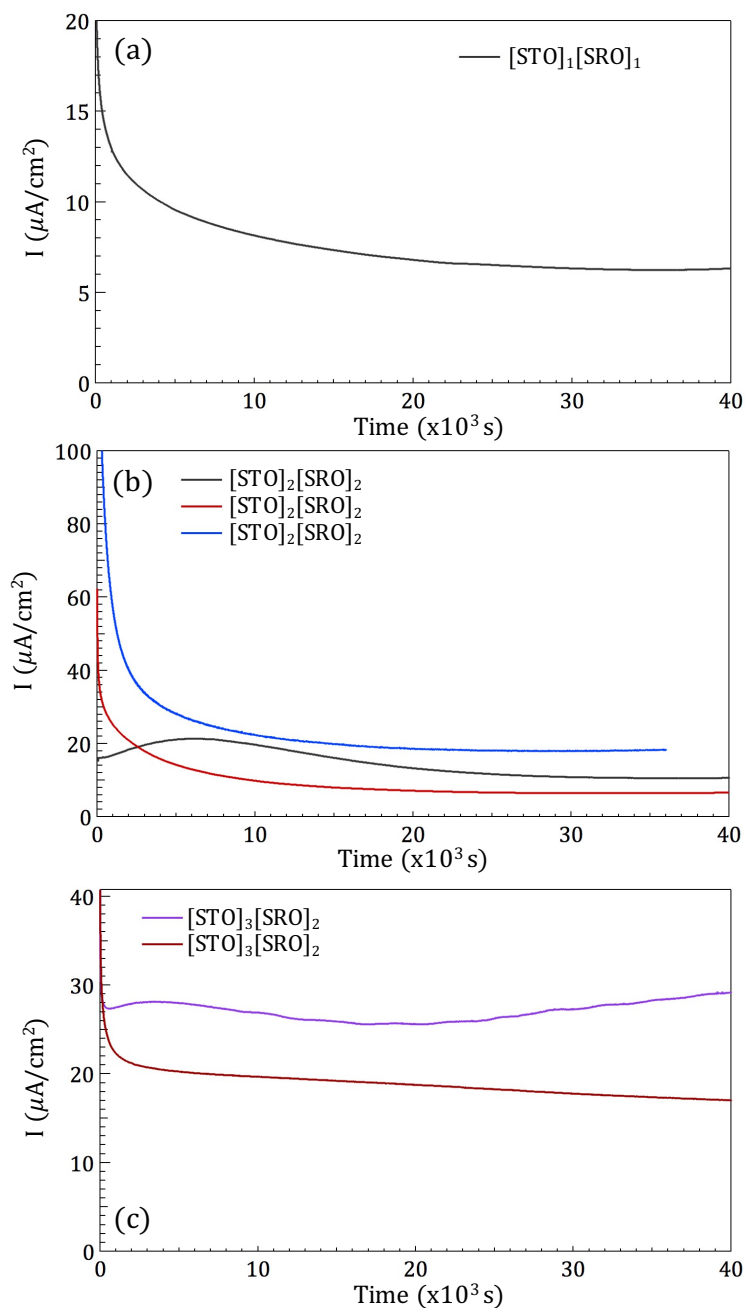


Extended Data Figure 16. Comparison of CV curves of the $[\text{STO}]_n[\text{SRO}]_m$ heterostructures for fixed (a) $m=1$ and (b) $m=2$. Scan rates are 10 mV/s.

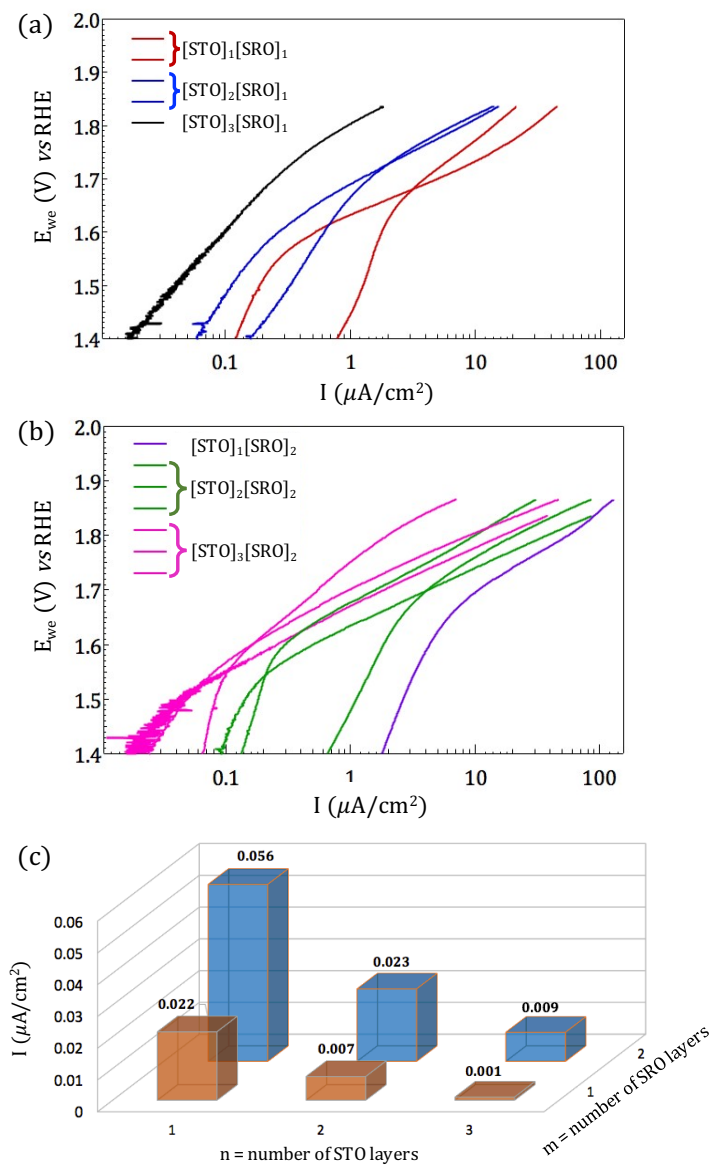


Extended Data Figure 17. CV curves of different heterostructures: (a) $[\text{STO}]_1[\text{SRO}]_1$, (b) $[\text{STO}]_2[\text{SRO}]_1$, (c) $[\text{STO}]_2[\text{SRO}]_2$, (d) $[\text{STO}]_3[\text{SRO}]_2$. Each CV represents a separate sample. Scan rates are 10 mV/s.

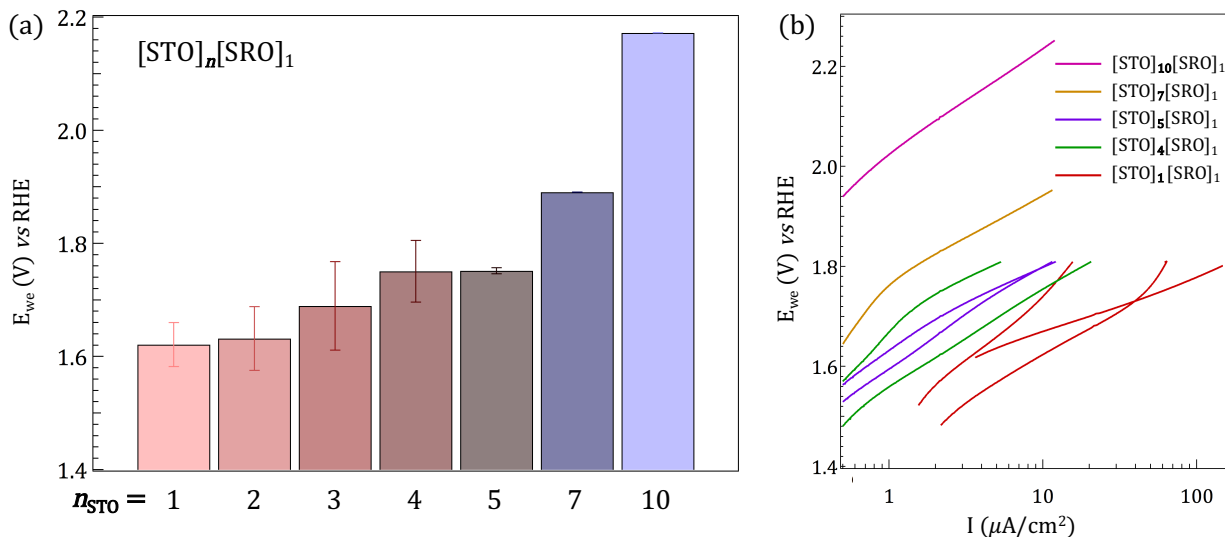
Below the potentiostatic stability curves are given for a few representative heterostructures. As of now, we do not know the reason behind the slow degradation of the heterostructures with $[\text{STO}]_1$. One possible explanation could be that this is a result of imperfect coverage of the SRO surface by the $[\text{STO}]_1$ protecting layer that can occur at the $[001]$ -step edges during the two-dimensional growth of the perovskite layers.



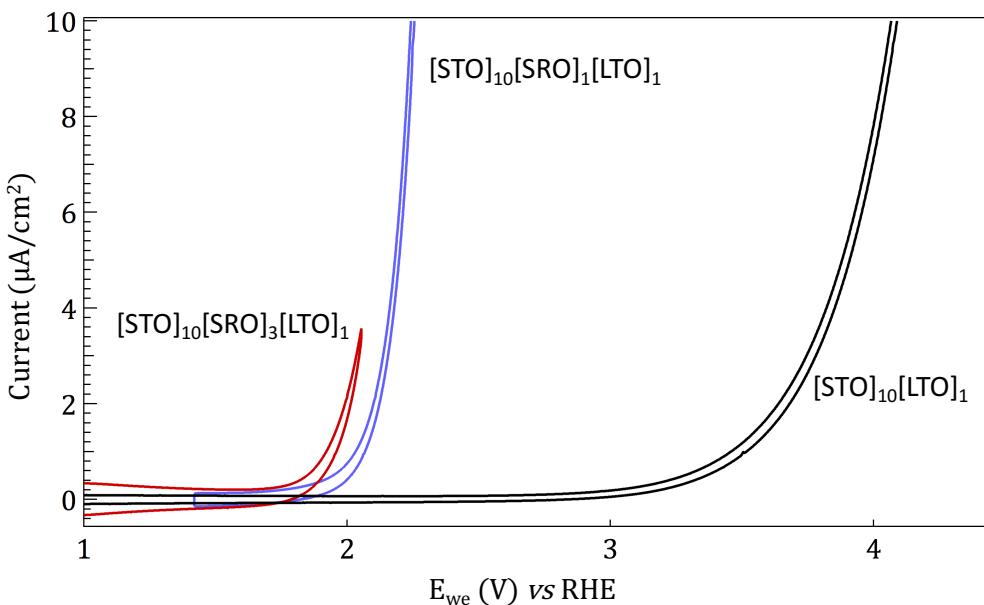
Extended Data Figure 18. (a) Prolong potentiostatic measurements for (a) $[\text{STO}]_1[\text{SRO}]_1$, (b) $[\text{STO}]_2[\text{SRO}]_2$, (c) $[\text{STO}]_3[\text{SRO}]_2$. Each curve represents a different sample. Scan rates are 10 mV/s.



Extended Data Figure 19. (a-b) Tafel plots for different $[\text{STO}]_n[\text{SRO}]_m$ heterostructures. (c) Averaged OER current extracted at the potential of 1.8 V vs RHE.



Extended Data Figure 20. (a) The potential at $i_{OER} = 5 \mu A/cm^2$ for the $[STO]_n[SRO]_1$ series; the error bars represent the standard deviation for a set of samples for a fixed n . For $n = 7$ and 10 we measured one sample in each case. Because of the limited number of samples, the standard deviation was calculated as $\sigma = \sqrt{1/N \sum_N (v_i - \bar{v})^2}$, where N – number of samples, v_i – the potential, \bar{v} – average potential for the particular set of samples ($n = \text{const}$). (b) Tafel slopes for the $[STO]_n[SRO]_1$ heterostructures with $n = 1, 4, 5, 7, 10$.



Extended Data Figure 21. Cyclic voltammetry of the $[STO]_{10}[SRO]_n[LTO]_1/Nb:STO$ heterostructures with $n = 0, 1, 3$.

Evaluation of the Gravimetric Activity

Herein we evaluate the gravimetric activity (A/g) of the heterostructures. The [STO]₂[SRO]₂ heterostructure has an areal current density of $\sim 100 \mu\text{A}/\text{cm}^2$ (at 0.6 V overpotential), which converts into a per-mass basis of ~ 53 A/g assuming a free-standing film. Considering that the target of a superior OER catalyst is to avoid or minimize the content of Ru and/or Ir, our system on a per-mass basis of active Ru has a high activity of ~ 185 A/g. For IrO₂ and RuO₂ thin films reported in literature, the current density on a per-area basis is 100-2,000 $\mu\text{A}/\text{cm}^2$, which converts into a per-mass basis of 6.0~120 A/g [for a 25 nm thick film, see *J. Phys. Chem. Lett.*, **5**, 1636-1641 (2014)].

Furthermore, the reported IrO₂ and RuO₂ nanoparticle catalysts have a current density on a per-mass basis of $\sim 7,500$ A/g and $\sim 11,000$ A/g, respectively [see *J. Phys. Chem. Lett.*, **3**, 399-404 (2012)]. If a nanoparticle with a core-shell architecture based on our heterostructure could be realized, we estimate the current density on a per-mass basis to be $\sim 6,500$ A/g, which is comparable to IrO_x and RuO_x nanoparticles. In addition, the estimated electrode performance of our system based on a typical specific surface area of an active oxide catalyst (area = 71 m²/g, mass loading 50 $\mu\text{g}/\text{cm}^2$ [see *J. Phys. Chem. Lett.*, **3**, 399-404 (2012)]) would be $\sim 3,500 \mu\text{A}/\text{cm}^2$.

References

1. Rong, X., Parolin, J. & Kolpak, A.M. A Fundamental Relationship between Reaction Mechanism and Stability in Metal Oxide Catalysts for Oxygen Evolution. *ACS Catalysis* **6**, 1153-1158 (2016).
2. Wu, K.T. *et al.* Surface chemistry and restructuring in thin-film La_{n+1}Ni_nO_{3n+1} (n = 1, 2 and 3) Ruddlesden-Popper oxides. *Journal of Materials Chemistry A* **5**, 9003-9013 (2017).
3. Tellez, H. *et al.* New perspectives in the surface analysis of energy materials by combined time-of-flight secondary ion mass spectrometry (ToF-SIMS) and high sensitivity low-energy ion scattering (HS-LEIS). *Journal of Analytical Atomic Spectrometry* **29**, 1361-1370 (2014).
4. Herger, R. *et al.* Surface structure of SrTiO₃ (001). *Physical Review B* **76**, 195435 (2007).
5. May, S.J. *et al.* Magnetically asymmetric interfaces in a LaMnO₃/SrMnO₃ superlattice due to structural asymmetries. *Physical Review B* **77**, 174409 (2008).
6. Bern, F. *et al.* Structural, magnetic and electrical properties of SrRuO₃ films and SrRuO₃/SrTiO₃ superlattices. *Journal of Physics: Condensed Matter* **25**, 496003 (2013).
7. Xu, P. *et al.* Reversible Formation of 2D Electron Gas at the LaFeO₃/SrTiO₃ Interface via Control of Oxygen Vacancies. *Advanced Materials* **29**, 1604447-n/a (2017).
8. Comes, R.B. *et al.* Probing the Origin of Interfacial Carriers in SrTiO₃-LaCrO₃ Superlattices. *Chemistry of Materials* **29**, 1147-1155 (2017).
9. Monkman, E.J. *et al.* Quantum many-body interactions in digital oxide superlattices. *Nature Materials* **11**, 855 (2012).
10. Chen, Y.Z. *et al.* Extreme mobility enhancement of two-dimensional electron gases at oxide interfaces by charge-transfer-induced modulation doping. *Nature Materials* **14**, 801 (2015).

11. Chang, S.H. *et al.* Functional links between stability and reactivity of strontium ruthenate single crystals during oxygen evolution. *Nature Communications* **5**, 4191 (2014).
12. Marshall, M.S.J., Newell, D.T., Payne, D.J., Egdell, R.G. & Castell, M.R. Atomic and electronic surface structures of dopants in oxides: STM and XPS of Nb- and La-doped SrTiO₃(001). *Physical Review B* **83**, 035410 (2011).